Biophysical Journal Volume 65 July 1993 149-163

Structure of the Extracellular Surface of the Gap Junction by Atomic Force Microscopy

Jan H. Hoh,*‡ Gina E. Sosinsky,§ Jean-Paul Revel,‖ and Paul K. Hansma*
*Department of Physics, University of California, Santa Barbara, California 93106 USA; §Rosenstiel Center, Brandeis University, Waltham, Massachusetts 02254 USA; and ‖Division of Biology, California Institute of Technology, Pasadena, California 91125 USA

ABSTRACT The extracellular surface of the gap junction cell-to-cell channels was imaged in phosphate-buffered saline with an atomic force microscope. The fully hydrated isolated gap junction membranes adsorbed to mica were irregular sheets ~1–2 μm across and 13.2 (±1.3) nm thick. The top bilayer of the gap junction was dissected by increasing the force applied to the tip or sometimes by increasing the scan rate at moderate forces. The exposed extracellular surface revealed a hexagonal array with a center-to-center spacing of 9.4 (±0.9) nm between individual channels (connexons). Images of individual connexons with a lateral resolution of <3.5 nm, and in the best case ~2.5 nm, were reliably and reproducibly obtained with high-quality tips. These membrane channels protruded 1.4 (±0.4) nm from the extracellular surface of the lipid membrane, and the atomic force microscope tip reached up to 0.7 nm into the pore, which opened up to a diameter of 3.8 (±0.6) nm on the extracellular side.

INTRODUCTION

The gap junction is a specialized region of the plasma membrane with an array of cell-to-cell channels (1). Activity of the channels is manifested by the ability to pass small molecules (<1 kDa) or provide a low-resistance electrical pathway between cells (2). Several biological functions have been proposed for the cell-cell communication mediated by gap junctions, including transmission of electrical synaptic signals, conduction of myocardial cell action potentials, coordination of smooth muscle contraction, regulation of growth control, transmission of developmental signals, and maintenance of metabolic homeostasis (for reviews see Refs. 2–4).

As with many membrane proteins, determining the structure of the gap junction has been a formidable task. That the channel can be isolated in large two-dimensional arrays (for a review see Ref. 5) has been a great advantage for structural analyses by x-ray diffraction and electron microscopy (6–9). However, disorder in the arrays has limited the resolution of these approaches to close to 2 nm, and the cytoplasmic carboxy terminus is apparently so disordered as to be invisible in the images obtained by these approaches (for a review see Ref. 10). In the current models six protein subunits (connexins) form a hexameric structure (connexon) in each membrane. Connexons are 6–7 nm in diameter with a pore through the center that is ~2 nm at its narrowest point. The center-to-center spacing between the channels varies from less than 8 nm to more than 9 nm depending on the concentration of detergent used during isolation (11). Two connexons interact head to head to form a cell-to-cell channel with a 2–3-nm gap between the membranes of apposing cells.

The extracellular domains of the connexins are composed of two ~40 amino acid loops, with a conserved set of three cysteines in each loop (for reviews see Refs. 12–15). For connexin-32 (Cx32) and connexin-43 (Cx43) it has been shown that these cysteines form at least one and possibly three disulfide bonds between the loops (16, 17). There are no interprotein disulfide bonds between connexins or between connexons. The extracellular surface of the gap junction has been imaged by deep etch freeze fracture of chemically split gap junctions (18), but there is little further structural information on the organization of these extracellular domains.

The atomic force microscope (AFM; also called scanning force microscope) is a relatively new instrument (19) for imaging biological surfaces in aqueous environments (for reviews see Refs. 20–22). It has been used to image the membrane proteins in purple membranes from *Halobacterium halobium* (23) and gap junctions (24–26) in physiological salines and the hexagonally packed intermediate layer of *Deinococcus radiodurans* (27) and metal-coated bacterial S-layers (28) in air. The AFM can also be used as a tool for micromanipulation of biological material (24, 29–31).

We have used the AFM to dissect isolated gap junction membranes and image the extracellular surface of fully hydrated individual connexons under near-physiological conditions. The surface topography determined by this approach is consistent with general aspects of current models but also reveals features not previously observed.

MATERIALS AND METHODS

Gap junction isolation

Twelve Sprague-Dawley rats (150–200 g; Simonsen Laboratories, Gilroy, CA, or Harlan Sprague-Dawley, Indianapolis, IN) were usually used to

---

Received for publication 10 October 1992 and in final form 5 January 1993.

Address reprint requests to Dr. Jan H. Hoh.

‡*Present address:* M. E. Müller Institute at the Biocenter of the University of Basel, Klingelbergstraße 70, CH-4056 Basel, Switzerland.

0006-3495/93/07/149/15 $2.00

obtain gap junction preparations. Rats were killed by cervical dislocation, and the livers were perfused with normal saline through the spleen after cutting the renal vein. The livers were homogenized in ice-cold 1 mM $NaHCO_3$ (BB) buffer, pH 8.2, with 1 mM phenylmethylsulfonyl fluoride (PMSF) with a tissuemizer (Tekmar Ultra Turrax, SDT-182 EN) for two bursts of 10 s. Homogenization was carried out after the removal of every three livers to minimize proteolytic degradation. The homogenate was then diluted to 1200 ml with BB/PMSF and filtered through 16 layers of cheesecloth. The filtrate was centrifuged at 11,000 rpm (16,000 × g_{av}) in a Sorvall GSA rotor for 50 min at 4°C. The supernatants were aspirated, and about 50 ml of 5 mM Tris-(hydroxymethyl)-aminomethane pH 10 (Tris10) with 1 mM PMSF was added to each bottle. The loose fluffy portion of the pellet was removed by gently swirling the bottles, taking care not to disturb the harder core of the pellet. These fluffy parts of the pellets were pooled and diluted to 600 ml with Tris10/PMSF and homogenized for a few seconds with the tissuemizer. Six hundred ml of 1.1% *n*-lauryl sarcosine (sarkosyl) in Tris10/PMSF was slowly stirred in at room temperature. The solution was stirred for 10 min, after which it was centrifuged at 11,000 rpm in a Sorvall GSA rotor for 50 min at 18°C. The supernatants were gently aspirated, and the top parts of the pellets were resuspended in 40 ml of 0.3% sodium deoxycholate (DOC) in Tris10 by 4 or 5 strokes of a Dounce homogenizer (pestle B; Wheaton). Two discontinuous sucrose gradients were prepared by successively layering 8 ml 49% (w/v) sucrose in Tris10/DOC, 10 ml 35% (w/v) sucrose in Tris10/DOC, and 20-ml of sample. The gradients were centrifuged at 25,000 rpm (81,000 × g_{av}) in a Beckman SW27 or SW28 rotor for 1 h at 18°C. Gap junctions were collected at the 35/49 interface, diluted with 2–3 volumes of Na_2CO_3 (pH 11), and centrifuged at 25,000 rpm for 20 min. The pellets were collected in 0.5 ml distilled water or phosphate-buffered saline (PBS; 137 mM NaCl, 2.7 mM KCl, 1.5 mM KH_2PO_4, and 4.3 mM Na_2HPO_4 at pH 7.2) and stored at 4°C for several days or −20° to −80°C for longer periods. Purity of the preparation was determined by gel electrophoresis and electron microscopy. Quantitative densitometry of gels showed that the yields of gap junction protein from this protocol were typically 2–3 μg of Cx32/g liver.

Sample preparation for microscopy

Disks (12-mm diameter) of ruby muscovite mica (Mica New York Corp., New York, NY) glued with epoxy to magnetic stainless steel punches (10-mm diameter, 0.9 mm thick) were cleaved to expose a clean surface. An aliquot (10–20 μl, 2–6 μg of Cx32) of gap junctions was immediately pipetted onto the surface and allowed to adsorb for 2 to 10 min. The surface of the mica was then rinsed 3 to 5 times with several hundred μl of PBS or water. Alternatively, the mica was wetted with PBS before adsorbing the gap junctions, with no obvious differences. The samples described here were imaged within hours, but storage for several weeks at 4°C in PBS did not appear detrimental.

Atomic force microscopy

A NanoScope III AFM (Digital Instruments, Santa Barbara, CA) was used for most experiments, and a NanoScope II was used occasionally. The microscope was equipped with a "J" type scanner with a *xy* range of 120 μm and a *z* range of 3.6 μm, or an "F" type scanner with an *xy* range of 17 μm and a *z* range of 4 μm. The sample was mounted in a standard commercial fluid cell. To avoid loading the piezo scanner and thus distorting the image, the o-ring was not used.

Operation of the AFM is a dynamic and interactive process, requiring constant attention to many parameters. Because the particular parameters vary greatly between experiments, in part because of tip and cantilever variability, it is neither useful nor practical to report the exact conditions for each image. Instead, ranges for most settings are described as a guide, and specific parameters are mentioned only when deemed particularly important. The scan frequency was 5–10 Hz (corresponding to tip speeds of about 1 to 1000 μm/s), integral gain control of the feedback circuit was 3 to 8, proportional gain was 0 to 1, and all scan directions (up/down and back/forth) were used. The scan angle was sometimes adjusted to reduce frictional contribution to the image by minimizing the separation of traces in the scope mode, usually to between 60° and 90°. The *x*-round was set to 0.5, causing the tip to move 25% outside the displayed image on both sides in *x*. All other parameters were zero or default settings. Imaging force was determined using force curves (32–34), although sometimes the force was minimized by simply lowering the set point until the tip pulled off the sample and then re-engaging at a set point just above the liftoff value. The latter is practical only if the adhesion between tip and sample is very small. Images were acquired at 512 pixels (400 with the NanoScope II) in *x* and *y*. (For further details and general operation principles of the AFM see Refs. 21, 22, and 35.)

All AFM images (except Figs. 1 *b* and 2) were acquired in constant force mode (i.e., "height mode"), so the gray scale corresponds to the height of the *z* piezo required to maintain a constant cantilever deflection. In Figs. 1 *a* and 2 the gray scale corresponds to actual cantilever deflections with the

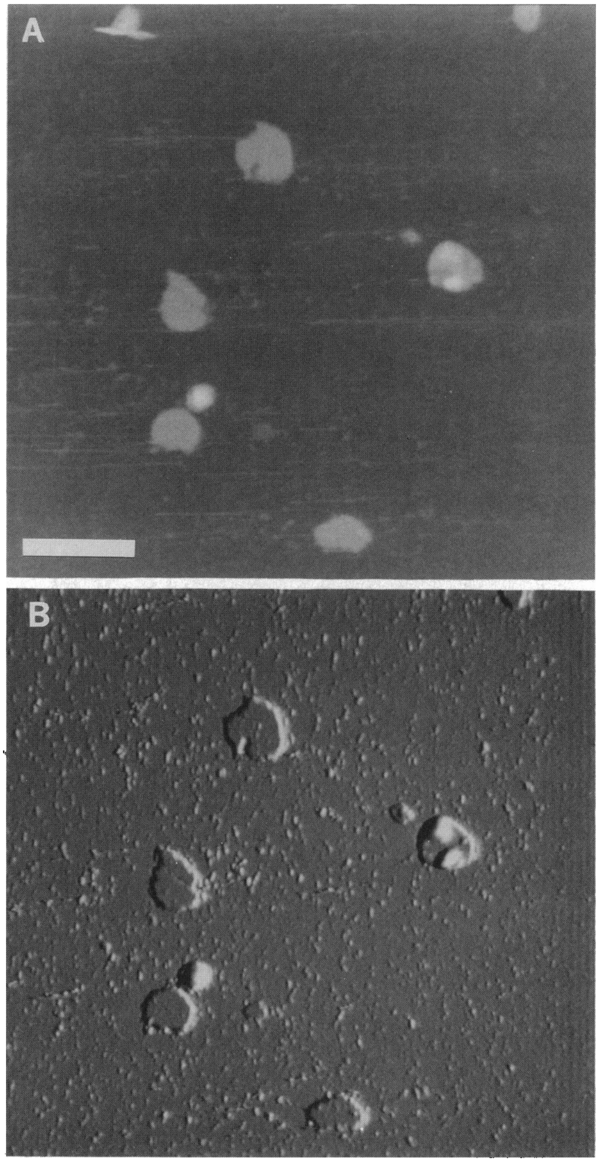

FIGURE 1 AFM image of isolated rat liver gap junction membranes in PBS. (*a*) A constant force image shows that these membranes have the size and distribution of isolated gap junctions (cf. Ref. 5) and are 13.2 nm thick. (*b*) Separate image of the same field taken in error signal mode accentuates high-frequency features such as edges and the extraneous material adsorbed to the mica. The nature of this material is unknown, although glycogen is a common contaminant in our preparations. Bar = 2.5 μm.

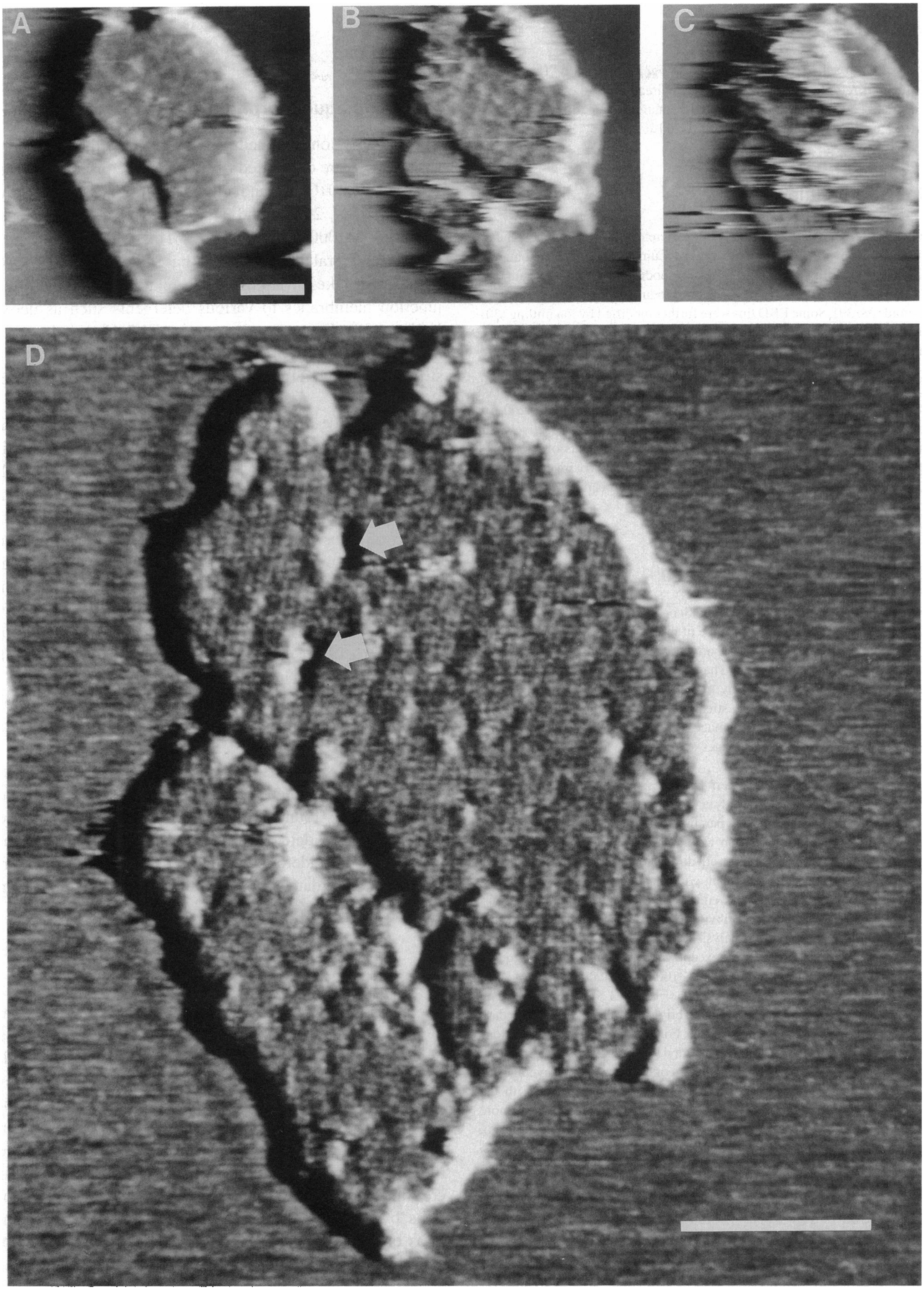

FIGURE 2 Dissection of a gap junction plaque adsorbed to mica (images are in error signal mode). (*a*) This plaque was scanned at 8 Hz over a 2 μm × 2 μm area at low force (near 1 nN). Under these conditions the membrane appears 13.2 nm thick and is stable for at least dozens of scans. (*b–c*) As the force applied by the tip is increased the top membrane becomes unstable and is removed. (*d*) This exposes the extracellular surface of the lower bilayer (which measures an average of 6.4 nm), with a hexagonal array of particles spaced 9.4 nm center-to-center. Holes in the membrane (*arrows*) appear to result from material trapped between the plaque and the mica during adsorption (26). (*a–c*) Bar = 150 nm. (*d*) Bar = 150 nm. Pixel size in (*d*) is 2 nm.

feedback loop active, referred to as error signal mode (36). The x and y orientations refer to the fast and slow scan directions of the image, respectively, and have no relation to sample orientation. The z direction reflects surface features perpendicular to both x and y.

Tips and cantilevers

Several different cantilever types with different tips were used. Standard silicon nitride cantilevers with integrated pyramidal tips (37) were obtained from Digital Instruments. These were also modified by electron beam deposition (EBD) as previously described to produce a microtip on top of the pyramid (38, 39). Some EBD tips were further modified by ion milling (30). Silicon cantilevers with integrated conical tips were from Park Scientific (Sunny Vale, CA).

Cantilever spring constants usually reported are from theoretical calculations (37). To estimate forces we have used the values 0.2, 0.04, and 0.03 N/m for V-shaped cantilevers 120 μm long and 15 μm wide legs, 200 μm long and 36 μm wide, and 185 μm long and 18 μm wide, respectively. All cantilevers are roughly 0.5 μm thick. Direct measurements of some cantilever spring constants show that these numbers are approximately correct, although variations of at least a factor of two have been observed for the same cantilevers of the same type (40, 41).

Image display and processing

Images were displayed using the NanoScope software or the NIH Image program (except Fig. 8). The pixel size of the original data is given in units of nm/pixel. This is particularly important for electronically magnified images, since the NanoScope software has an automatic interpolation function. Many images were "flattened" by offsetting each scan line to the same average z value. This reduces the streaking caused by the tip skipping and other line noise, but for uniform images with little variation in z does not significantly alter the data. All images are otherwise unfiltered unless specifically indicated.

The calibration of piezo scanners is at present very difficult. Accurate measurements are available for only a few preparations studied, for which our scanners were recalibrated and parameters adjusted for the length scales used. When the scanner calibration was not adjusted, we found that structures generally appeared larger in all dimensions. However, the relative measurements were still in agreement with those given here. For the measurement of membrane heights, several points along several cross sections on each membrane, excluding the obviously bumpy regions, were averaged.

For filtering and correlation analysis the Nanoscope III image files were converted to VAX-compatible files (except where noted), and all subsequent computations were carried out on VAX 3100 work stations. Images were first scaled by removing all values above or below 3 SDs from the mean. This scaling procedure usually eliminated bright scan artifacts and very dark features caused by holes in the membrane. Fourier transforms and filtrations of the images were then carried out as previously described (42–44). Due to distortions in the lattice and individual connexons, Fourier averages of the quasi-crystalline hexagonal areas tended to be inconsistent with the original images. Correlation averaging procedures (see Ref. 42 for more detailed descriptions of these procedures as applied to gap junction lattices), which are less dependent on the lattice order and can select for the best areas, were generally more successful. Original references for the high-pass and low-pass filtered images were chosen for clarity and presence of substructure in the connexons. Averages contain the sum of 25 subareas the size of the reference.

Rotational power spectra for individual connexon images were computed according to the method of Crowther and Amos (45). The resolution of the correlation averages was assessed by computing the spectral signal-to-noise ratio (SSNR) for each pixel in our averages (46). We based our estimate of the resolution for the connexon contribution to the image by looking at peaks for which the SSNR is >4 and by ignoring the periodic component of the scan repeat, which extends to the edge of the SSNR map.

RESULTS

General plaque morphology

The gap junctions isolated from rat liver by the method described here are composed (>90%) of one principal protein with M_r 28,000 (Cx32) and minor amounts of two breakdown products of M_r 26,000 and 24,000, and very small amounts of the M_r 21,000 protein (Cx26). This isolation method is similar to several other detergent-based isolation methods (5, 47–49) that take advantage of the relative resistance of gap junction membranes to various detergents such as deoxycholate (50). Electron microscopy (EM) shows that these membranes are highly purified, with few contaminating structures detected by negative staining (data not shown; cf. Ref. 24).

Atomic force microscopy of isolated hydrated gap junctions on mica in PBS reveals membranes with characteristics similar to those seen by EM (Fig. 1). These are irregular membrane sheets (plaques) of ~1 to 2 μm in diameter. At low applied vertical force, near 1 nN, these are stable for dozens of scans (at least an hour, as long as they have been observed). Significant amounts of extraneous material are often adsorbed to the surface. This material is weakly bound and is usually swept away during prolonged imaging but sometimes becomes trapped beneath the membranes during adsorption, causing undulations or bumps on the surface. The plaques have a measured thickness of 13.2 (± 1.3, $n = 15$) nm, which is slightly less than measurements from previous force microscopy (24) and cross-sectional measurements from EM (51).

The cytoplasmic surface of the gap junction plaques has been closely examined for regular features or substructure and is generally found to be featureless (Fig. 2 *a*). However, we have recently detected a periodic structure typical of connexon spacing under some conditions, although it is poorly resolved. These data are beyond the scope of this report and will not be discussed further.

Dissection of gap junction membranes

The dissection of gap junctions in solution adsorbed to glass by increasing the force applied to the tip has been described previously (24, 25). This process exposes the extracellular surface of one-half of the gap junction membrane by removing the top bilayer (Fig. 2). The dissection of gap junctions on mica was performed in a similar way, by increasing the vertical force, as determined from force curves, applied to the sample. Dissection can also be accomplished by increasing the scan rate at moderate forces or, in some situations, by decreasing the feedback loop gains. As for gap junctions on glass, junctions on mica are generally very stable near 1 nN, but the top membrane was usually removed at forces of >10 nN. However, the applied vertical force needed to separate the two membranes varied significantly (by more than a factor of 2) between experiments, suggesting that other factors such as, perhaps, tip structure are important.

The membrane remaining after dissection appears to be 6.4 (±0.6, $n = 8$) nm thick (as measured from the mica to the top of the connexons), a measurement that is consistently slightly less than one-half of the full thickness of the gap junction. The exposed extracellular surface of the gap junction has features that, at moderate magnification are seen as a clear periodic height modulation (Fig. 2 *d*). The pattern of this modulation is hexagonal, with a center-to-center spacing of 9.4 (±0.9 nm, $n = 7$) nm as determined from the Fourier transform, which is consistent with the spacing of individual connexons, although slightly larger than typical EM measurements of negatively stained preparations of 8 to 9 nm (8, 44). The value reported here for connexon spacing is at present limited by the calibration of the AFM, which we estimate to be ±10%. The mica around the membrane is smooth on this scale, demonstrating that the hexagonal pattern does not arise from the mica substrate. The hexagonal pattern is also similar to that seen with gap junction plaques on glass (24).

Holes are often found in the membrane remaining after the dissection (Fig. 2). We have previously discussed in more detail the possibility that these surface undulations resulting from material trapped under the membrane reduce adhesion between the protein and the mica substrate (26). During dissection weakly attached patches of the bottom membrane in these areas are removed.

Connexon surface structure

At high magnification, significant substructure is seen in dissected gap junctions on mica. The most detailed images are obtained at very low force. Fig. 3 *a* shows a portion of a dissected gap junction plaque acquired during a drift toward lower force. A well-resolved array of channels is seen near the bottom of the image, and the array of channels disappears gradually toward the top as the tip lifts off the surface. Magnification of several areas of this plaque reveals significant detail in the structure of the individual connexons (Fig. 3 *b–c*).

High-resolution images of connexons with substantial detail can now be obtained routinely with a good tip (Figs. 3 and 4). These images reveal a number of morphologies ranging from relatively amorphous to pentagonal or hexagonal. Many connexons exhibit height modulation at the periphery of the channel in the several tenths of nanometer range. Because of tip shape contributions to the image, the connexon diameter was measured at the highest point from the surface. At this point, the average connexon we have examined is 3.8 (±0.6, $n = 22$) nm across (Fig. 5). Many connexons appear to have a missing subunit in one corner, producing a C-shaped appearance. This may reflect a true structural feature of these connexons or a defect generated during the dissection.

The apparent depth of the pore at the center of each connexon measured by the AFM varies from undetectable to about 0.7 nm. These measurements are lower limits since the width of the tip prevents it from entering and probing the whole depth of the pore. The same problem arises when measuring the height of connexons above the lipid membrane from the space between connexons. In the latter instance, however, the problem is circumvented by measuring connexon heights above the membrane at the edge of the array (see below).

Channel arrays are usually stable under repeated scanning at low force. Fig. 6 shows a series of four sequential scans over the same area. Since the images were acquired in only one scan direction (right to left), the tip actually moved over the entire area eight times. The overall lattice and much of the fine structure are stable, although there is some variation in details.

In many of the high-resolution images shown here, some features of the connexon such as the pore are not clearly visible to the eye. A simple high- pass filter (Fig. 7) significantly enhances these features, revealing a pore in most connexons (see Fig. 6 *c*, for example).

Correlation averaging and Fourier analysis

Correlation averaging is an image-processing procedure that does not depend on lattice order to produce self-consistent averages (42, 52). The averages obtained from eight references chosen from a filtered image are consistent with each other in terms of general features (Fig. 8). While the substructure varies from connexon to connexon, the channel and the general appearance of connexon lobes are still apparent after averaging.

We computed the rotational power spectra (45) of the connexon images in Fig. 8 (*c–f*). The average sixfold azimuthal power for the four connexons shown is ~15% in Fig. 8 *c*, ~9% in Fig. 8 *d*, ~10% in Fig. 8 *e*, and ~8% in Fig 8 *f* (±2–6%). The average fivefold azimuthal power totals are ~13%, ~13%, ~7%, and ~7% (±2%) for Fig. 8 *c–f*, respectively. In Fig. 8, the connexon image with the highest sixfold azimuthal power is C1 (21%), and connexon D4 had the highest percentage of fivefold rotational power (19%). There are no striking differences between these measures of hexagonal versus pentagonal symmetry, and therefore there is no quantitative basis for assigning a subunit structure based on the images presented here.

Diffraction patterns of high-resolution images usually show reflections out to (2,0) and (1,1) (Fig. 6) with occasional weak spots as far out as (3,0) and (2,2). The resolution appears to be limited by disorder in the array, and in some cases by the individual units, which prevents the presentation of useful Fourier-averaged images. A useful gauge for determining the effective resolution of correlation averages is the spectral signal-to-noise ratio of Unser et al. (46). According to this criterion, the *xy* resolution of the connexon averages displayed in Fig. 8 was ~2.5 nm. Similarly, correlation averages computed from individual units in Fig. 6 *a* had a maximum resolution of ~3.0–3.5 nm, and correlation averages from another image (not shown) were also ~2.5–3.0 nm.

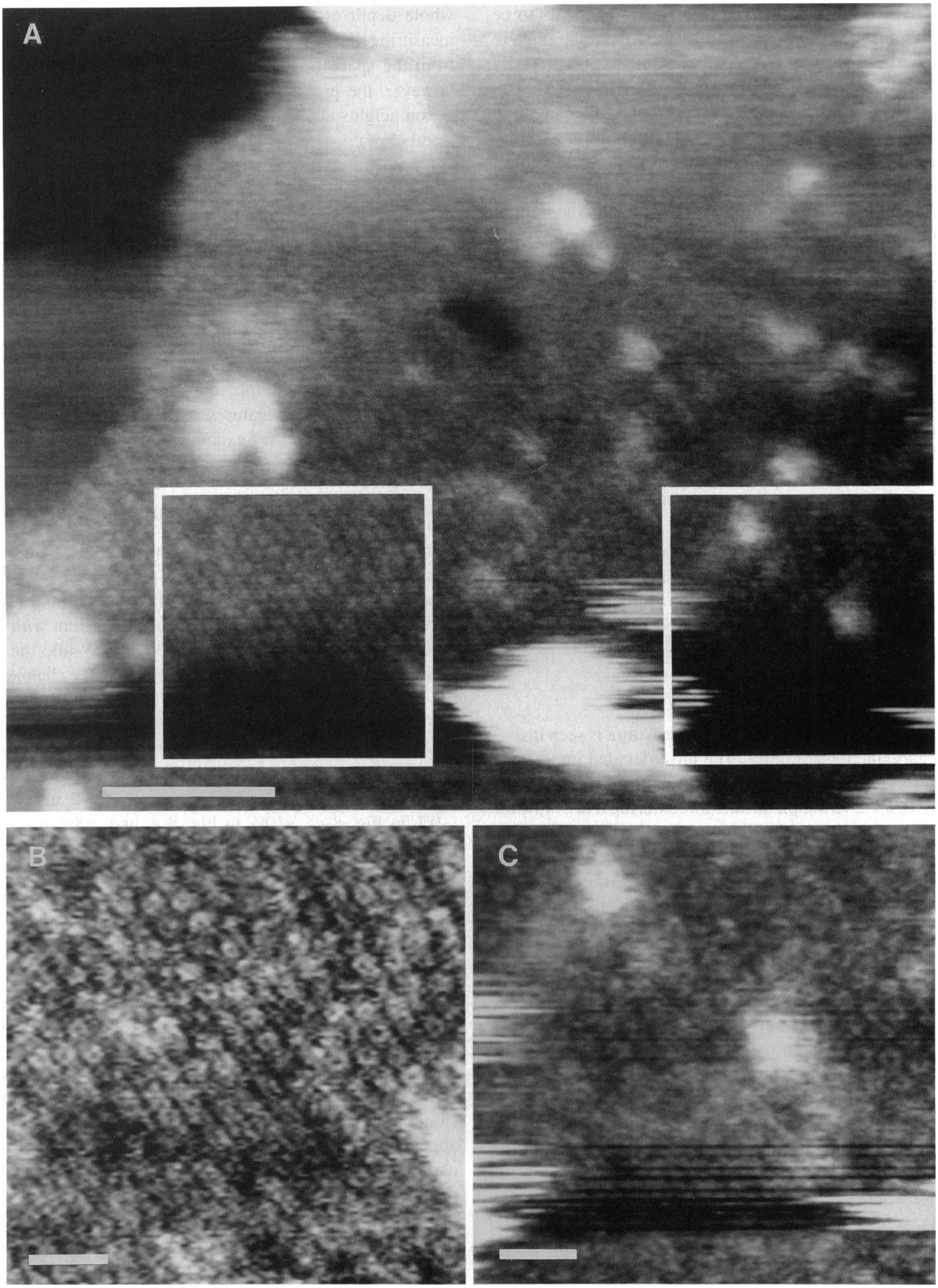

FIGURE 3 (*a*) AFM image of the extracellular surface of a dissected gap junction membrane. The image was taken with an ion-milled, electron beam-deposited tip in PBS during instrumental drift toward lower force. A clear hexagonal array of channels with a center-to-center spacing of 9.4 nm is visible near the bottom of the image. Toward the top of the image the force becomes so low that the tip begins to lose contact with the sample, resulting in a general fuzziness and loss of the hexagonal array. Magnification of regions to the (*b*) left of center and (*c*) right of center (shown at a slightly different contrast) shows details of the individual connexon surface topography. Several morphologies are visible, including hexagonal and pentagonal connexons. (Pixel size for all images = 1.2 nm.) (*a*) Bar = 100 nm. (*b–c*) Bar = 25 nm.

Asymmetric resolution

In many images the hexagonal lattice symmetry is somewhat obscured because one of the lattice axes is more prominent, a feature we call streaking (Fig. 2 *d*). This streaking does not appear to be an authentic feature of the gap junction but seems to result from an asymmetric tip. Some membranes show multiple domains resulting from a defect in the two-dimensional lattice (Fig. 9 *a*). With an asymmetric tip this can produce a relatively well-resolved array that is adjacent to another domain that shows streaking along one axis. In a computer simulation a simple model array that is "imaged" with an asymmetric tip produces a similar pattern with nearly identical diffraction patterns, supporting the suggestion that tip asymmetry is the source of this feature (Fig. 9 *b*).

Border to nonjunctional membrane

On many gap junction plaques a small region of apparently nonjunctional membrane is seen (Fig. 10). These regions usually exhibit a droplike shape and are 5 nm thick and contiguous with the gap junction proper. There is no substructure typical of the gap junction on the drop, and in fact the surface is smooth to within a few tenths of a nanometer. The origin of these regions is not yet understood, but their position, shape, and size suggest that they are naked lipid bilayers. At the border between the junctional and nonjunctional regions of the membrane the connexons extend above the nonjunctional membrane by 1.4 (± 0.4, $n = 8$) nm. To get an accurate value the height is measured as close to the border as possible. The component of the measured thickness due to the cytoplasmic domain of the junctional protein is probably not large, since trypsin-treated liver gap junctions have the same measured thickness as intact plaques (24) and there is no obvious slope in the nonjunctional membrane at the border that would result from a cytoplasmic contribution.

DISCUSSION

Plaque morphology

The general shape of isolated gap junctions in solution seen here is in good agreement with that seen in dehydrated (see, for example, Ref. 5) or frozen hydrated samples (9). The measured thickness of gap junctions on mica visualized by AFM is 13.2 nm, slightly smaller than values obtained by EM, which are near 15 nm (51). This discrepancy is consistent with substrate-dependent thickness measurements of purple membranes from *H. halobium* that have been reported to appear thinner on mica than on glass (23). The basis for

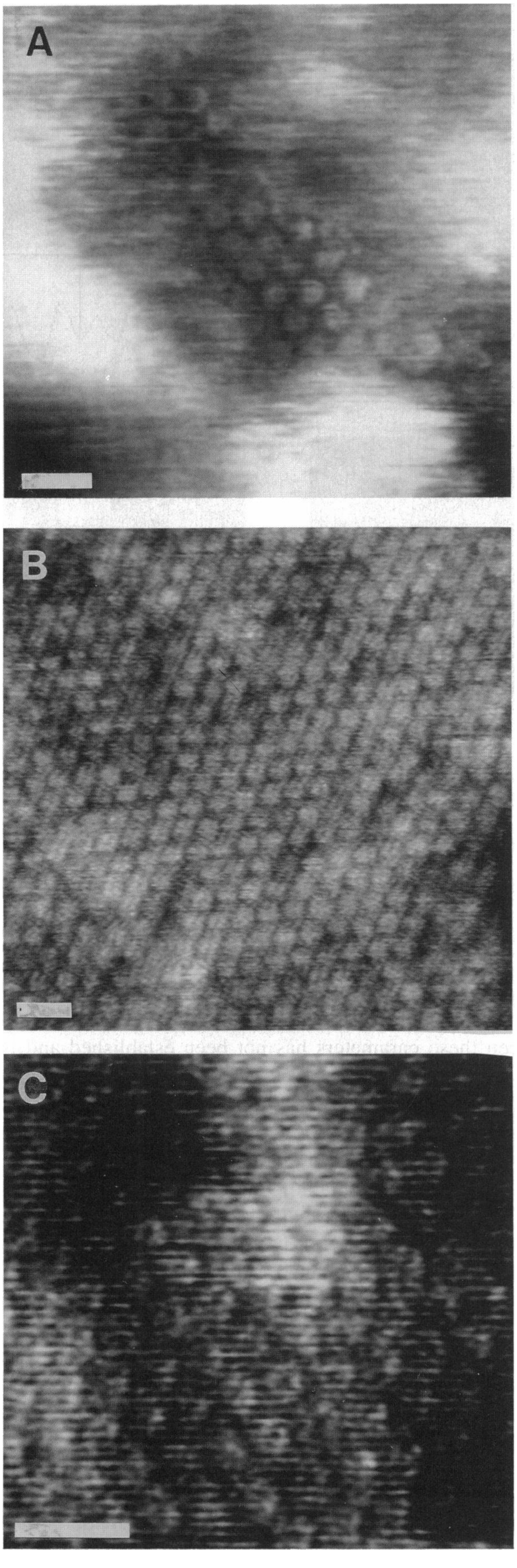

FIGURE 4 (*a–c*) AFM images of gap junction surfaces in solution from three experiments showing that high-resolution images can be obtained routinely, although there is significant variation in substructure. Since these images were acquired under similar conditions, we attribute this variation in structure to differences in the tips used (different for each image). This suggests that tip shape is resolution limiting. Bar = 20 nm.

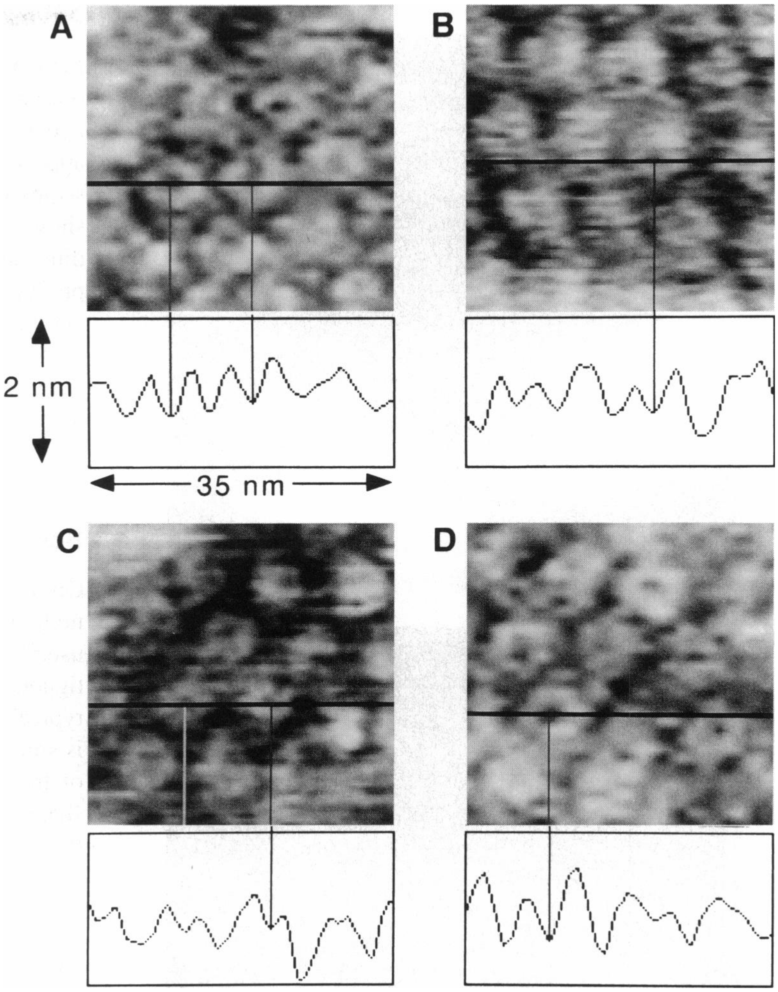

FIGURE 5 Cross sections through selected connexons. The apparent depth of the pore is at most 0.7 nm, suggesting that the tip is too broad to probe its whole length or that there is an obstruction. The diameter of the channels at the surface furthest away from the lipid membrane is 3.8 nm, in connexons with a clearly resolved pore. (*a*) Connexons from Fig. 3 *a*. (*b*) Connexons from Fig. 4 *b*. (*c*) Connexons from Fig. 4 *a*. (*d*) Connexons from Fig. 3 *b*.

this effect is not yet known, nor are all the factors that influence the height measurement fully understood. One effect that may be particularly important is friction, since this can cause a twisting of the cantilever perpendicular to the scan direction and thereby affect the apparent height. In addition the absolute height values described here depend directly on the calibration of the *z*-piezo, which is difficult to establish with certainty and at present is not compensated for nonlinearities. Although the absolute values are uncertain, the relative measurements of features of similar size (true for everything shown here) within the same image are accurate.

Plaques are stable under repeated scanning at low force (near 1 nN) with no apparent damage to the sample, but under commonly used imaging conditions the top membrane becomes unstable and is dissected away at forces near 10 nN. These force values reflect only the vertical force component near equilibrium as determined from force curves. During scanning the vertical force component changes as features are encountered, as reflected in the error signal (36). The magnitude of these transient changes will depend on many factors, including the response characteristics of the feedback loop. There are also horizontal (lateral/frictional) forces that will contribute to the dissection process. We find that the scan rate and feedback control are critical factors in the dissection and that increasing the scan rate or decreasing the gains to the feedback loop have the same effect as increasing the applied vertical force. The quantitative relationship between these parameters has not been established and is at present difficult to investigate since it appears to depend critically on the tip shape. Therefore the force values used to achieve dissection are for a narrow range of scan rates and gains and are to be seen as rough estimates.

The membrane remaining after dissection is consistently 0.2–0.3 nm thinner than half of the whole gap junction, suggesting that some sort of asymmetry in the plaque may be induced by surface contact. It is worth noting that Unwin and Zampighi (8) have described a deviation from the space group p622, indicating that the two halves of the membrane were not identical. They suggested that this arose from heavy metal stain drying at the edge of the membrane, although it would appear that this asymmetry could also be an effect of the interaction of the bottom of the membrane with the carbon support film. Surface-induced thinning of the bottom membrane has also been seen in cross sections of gap junctions adsorbed to carbon (Sosinsky et al., unpublished observations). Such surface effects have serious implications

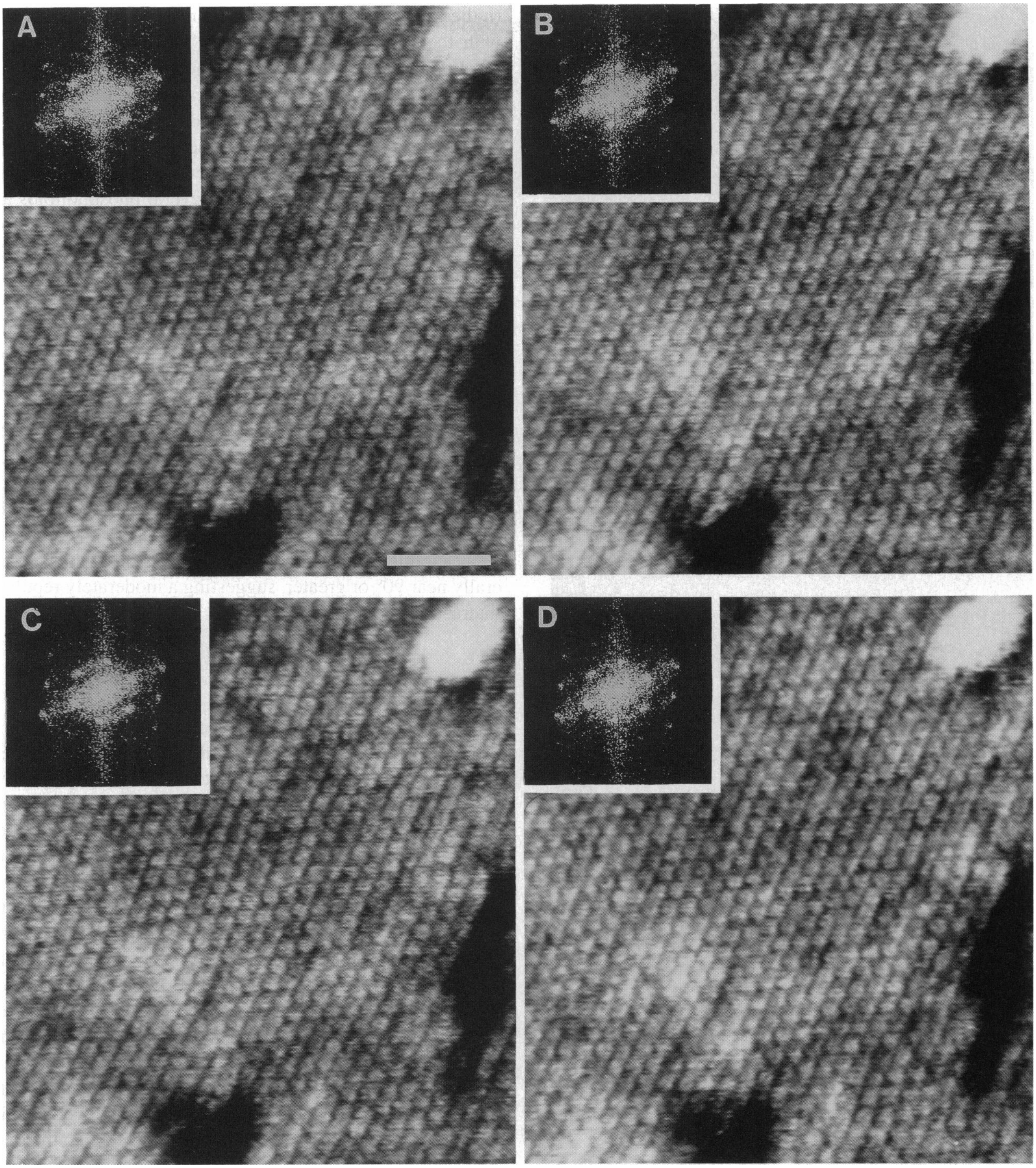

FIGURE 6 (*a–d*) Series of AFM images showing the stability of connexon substructure during repeated scanning. The scans were immediately sequential and therefore (*a*) and (*c*) are up scans and (*b*) and (*d*) are down scans. All scans were made with the tip moving from right to left. Because of piezohysteresis and bowing of the cantilever, scans in the same directions are expected to be more similar. The diffraction patterns demonstrate that the overall lattice structure is stable, although there is some variability in the fine structural details. Pixel size = 0.6 nm. Bar = 50 nm.

for the functional activity of these membranes adsorbed to a surface and raise concerns about how far from the surface this perturbation of structure propagates.

The adhesion between the gap junction membrane and the mica must be stronger than the interaction between the membranes in order for the bottom membrane to remain on the surface during a dissection and appears to be mediated primarily by electrostatic forces. Glutaraldehyde fixation has been shown to destabilize the interaction between a gap junction membrane and glass (24), presumably by reacting with

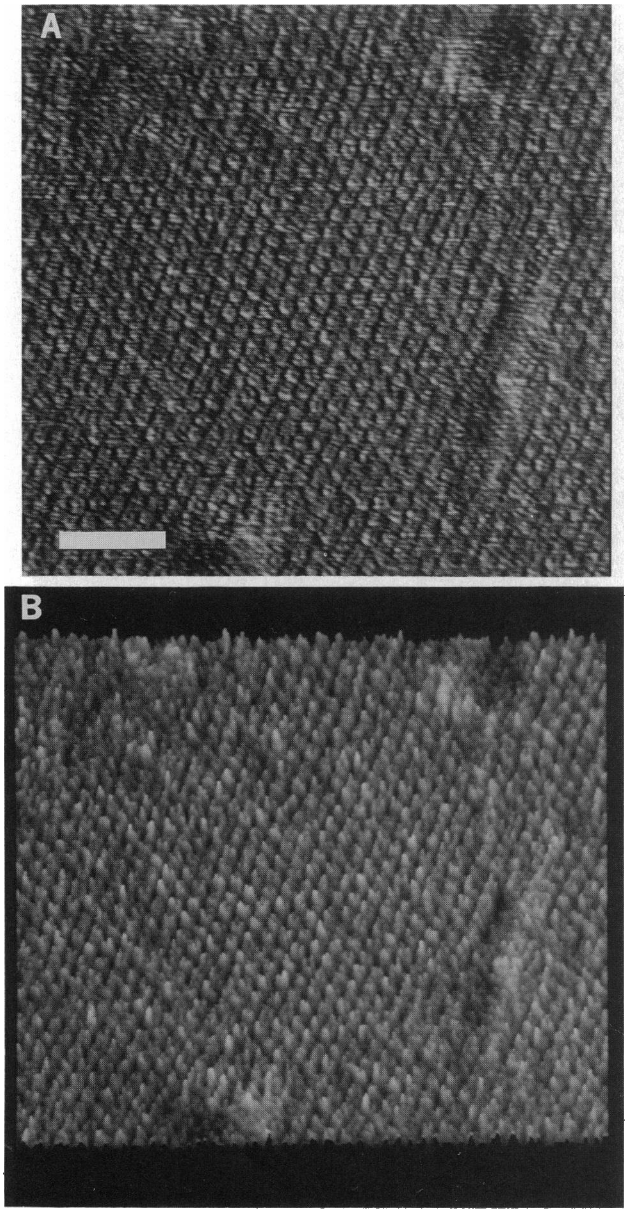

FIGURE 7 (*a*) A simple high-pass filter (after imaging, using the Nanoscope software) from Fig. 6 *c* reveals a pore in most connexons in this gap junction membrane, which are not otherwise clearly visible. (*b*) Surface plot of the same image. Bar = 50 nm.

positively charged amino acids such as lysine or arginine. Like glass, mica is a negatively charged surface and can interact strongly with positively charged amino acids in the protein. The lipid components of the gap junction are probably not in direct contact with the mica, and the nonjunctional lipids appear to adhere more weakly than the bottom half of the gap junction membrane (26). Also, since cleaved mica is atomically flat over large areas, surface roughness in not an important factor for the stable interaction between the gap junction membrane and mica.

The small structures, with a droplike shape in the plane of the membrane, at the edge of many gap junction plaques have several properties of lipid membrane. They are liquidlike (indicated by the shape), near 5 nm thick, and contiguous with the gap junction membrane. The origin of this nonjunctional membrane is at present not understood. They may represent nonjunctional plasma membrane that survives the detergent treatment or have formed during or after the isolation procedure. Nonjunctional membrane attached to gap junctions has been seen in fragmented plasma membranes (53). There are large amounts of several phospholipids and cholesterol in isolated rat liver gap junctions (54), and it may be that one or more of these segregates to the edge of the plaque during some manipulation such as storage, freezing, thawing, or adsorption to the mica.

The most obvious benefit of the edge views is that they provide a direct measurement of the connexon height above the lipid. However, the very characteristic droplike shape (see Fig. 10) of these regions raises the exciting possibility of determining interaction energies for lipids with connexons. The use of contact angles between liquids and surfaces to determine interfacial energies is a well-established technique in surface science and material research (55). In this case the lipid "droplet" on the edge of the gap junction forms a measurable contact angle in two dimensions, which is generally near 90° or greater, suggesting a moderately repulsive interaction.

Connexon structure

The structure of connexons has been described in detail by a number of groups. The most fruitful approaches have been based on x-ray diffraction of pellets of isolated gap junctions or electron microscopy of preparations that have been frozen or stained with heavy metals such as uranyl acetate or phosphotungstic acid. These approaches have led to two models that share many general features but differ particularly with regard to the mechanism of gating (9, 56). At present the resolution of these models is limited by disorder in the arrays to just below 2 nm. The structure of the connexons at the extracellular surface is relatively poorly characterized, particularly since the current models are based on reconstructions of the entire channel (i.e., two interacting connexons), which is then divided at the midpoint between the membranes to produce a single connexon. In the present work the upper half of the gap junction membrane is removed, leaving a single layer of connexons in a bilayer attached to the mica. Thus the extracellular aspects of the connexons' normally covered surface are imaged directly by the AFM, providing structural information that complements previous approaches.

The individual connexons of the gap junction measured here protrude 1.4 nm from the extracellular surface when measured from the edge of plaques (Fig. 10), which is in close agreement with the value deduced by dividing the size of the gap between the membranes (7, 8). The average pore size in these images is about 3.8 nm at the presumptive connexon-connexon contact site, which is substantially more than the ~2 nm that has been previously reported (8). There are several possible explanations for this discrepancy be-

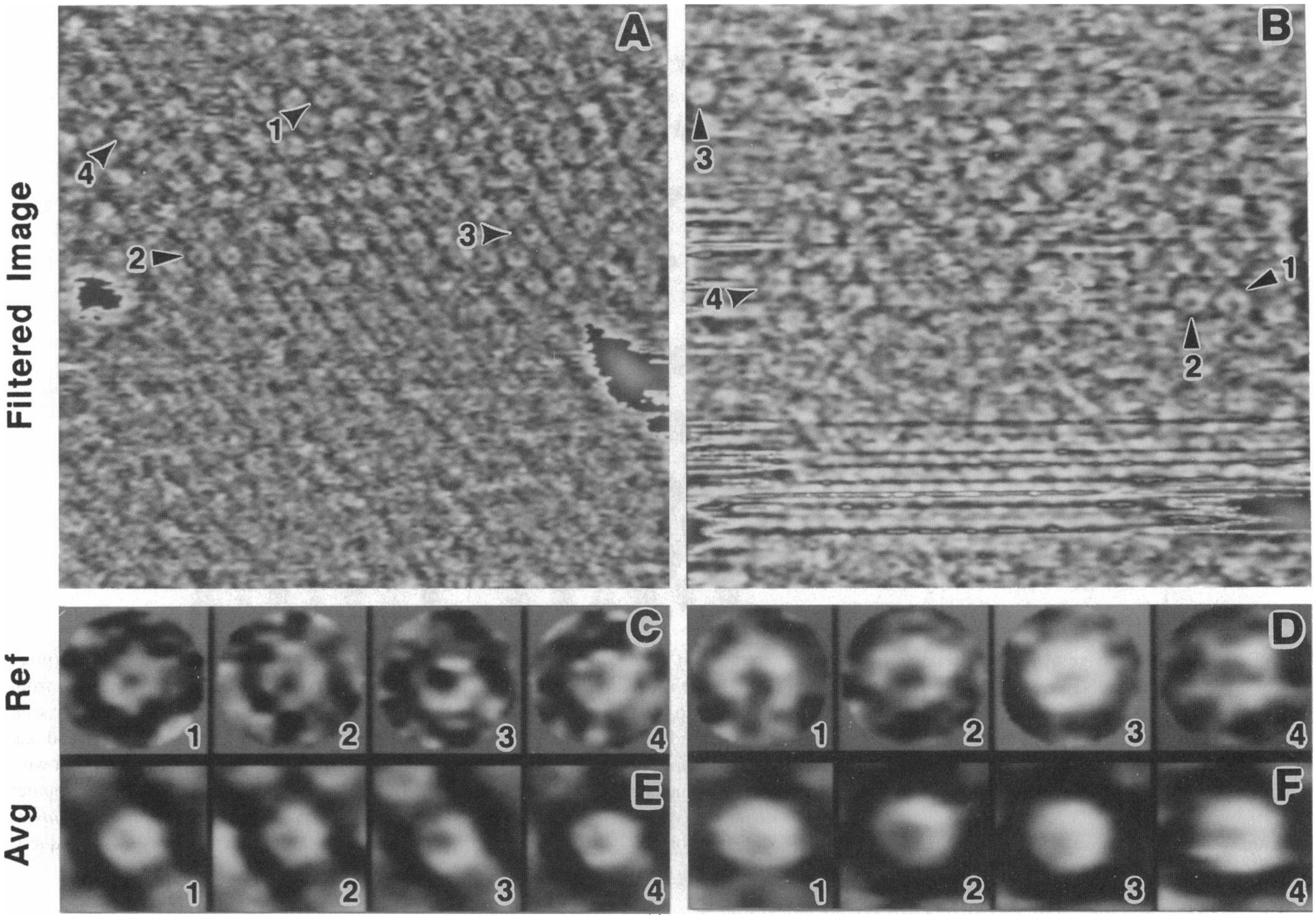

FIGURE 8 Filtered images and correlation averages obtained from AFM images. (*a-b*) The images shown in Fig. 3 were judged by eye to be the highest-quality connexon images and were high- and low-pass filtered (*a* is scaled 25% larger than *b*). References were chosen from the filtered images (*c* and *d*, arrows on filtered images). Corresponding correlation averages were calculated from the sum of 25 subareas (*e* and *f*). The pore is highly visible in the original references, and this structural feature is reflected in the averages, as are the lobes of the connexons.

tween these observations of the diameter of the pore. The different environment of the samples, such as substrate and composition of the imaging solution, is one possibility. It is also possible that certain parts of the protein, such as amino side chains, are "soft" relative to others and might be pushed out of the way by the tip, causing an artifactual broadening of the pore in the AFM image. Furthermore, the separated connexons may have a structure very different from that seen when they are together.

Beyond the pore and height above the lipid membrane the majority of connexons we have observed exhibit little or irregular substructure, but our best images show both hexagonal and pentagonal substructures. Quantitative analysis of rotational symmetry in the correlation averages does not clearly support either of these subunit arrangements. Many connexons also exhibit height modulation at their periphery, which suggests that the contact site between connexons in apposing membranes may not be smooth. One possible implication for this is that two connexons interlock like two cogs to form a cell-to-cell channel.

The resolution determined from the diffraction patterns, which clearly show all the reflections out to (2,0) and (1,1), is at least 4.7 nm in the plane (*xy*). However, this measure of resolution is limited by disorder in the array. Analysis of the spectral signal-to-noise ratio indicates that the resolution in the best images is ~2.5 nm, which is also evident from a simple visual inspection of some images (such as Fig. 5). The *z* resolution is coupled to the *xy* dimensions in that features must be sufficiently well separated in the plane for the differences in *z* to be observed. While we have not performed a formal analysis of the *z* resolution in our images, it is clear that for well-separated features the height is resolved to better than 0.2 nm (see, for example, Fig. 5).

Tip structure effects

The variations in connexon morphologies observed in different experiments are not fully understood. Conditions that can be controlled such as temperature, composition of imaging buffer, control of feedback loop, etc., are all similar or identical in the experiments described here. The most variable component between experiments is the structure of the tip. This is composed of both the large-scale structure described by the radius of curvature and the small features and

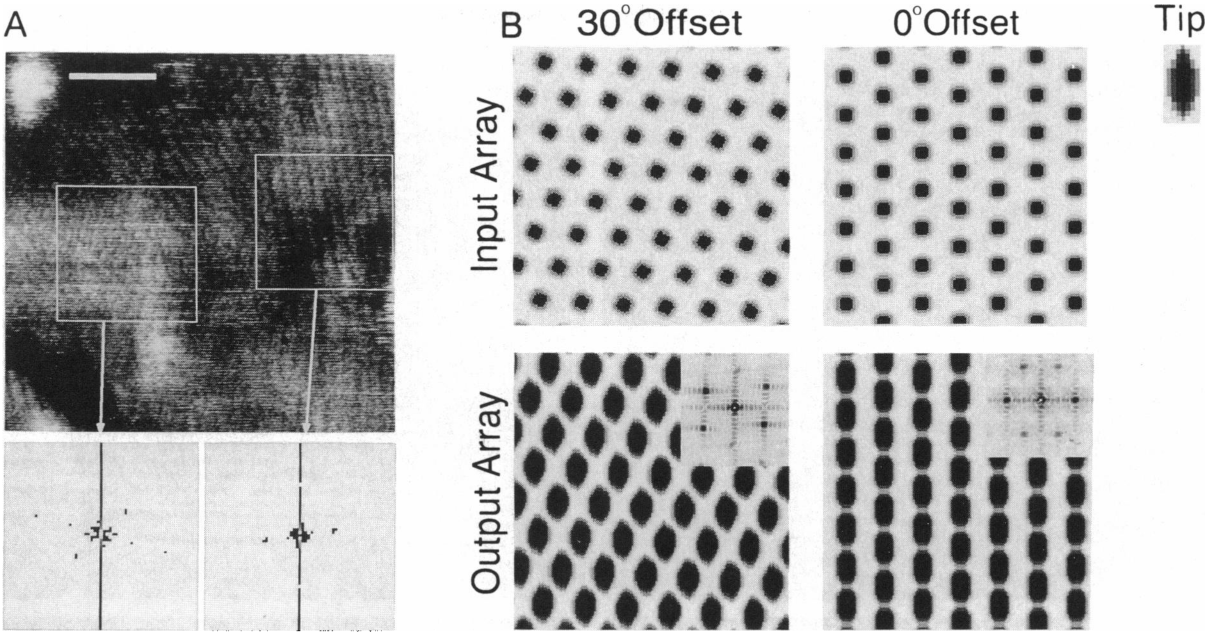

FIGURE 9 (*a*) AFM image of the extracellular surface of a gap junction membrane showing the array of connexons with a defect in the lattice (pixel size = 0.8 nm). This results in two domains, with the array on the left side rotated from that on the right by 29°. Fourier transforms were computed from 90 × 90 nm areas on the left and right side of the image. An asymmetric tip produces an apparent streaking of the array on the right, which is clearly seen by the prominent (1,0) reflection in the diffraction pattern. The left side produces two weaker spots at (1,0) and (0,1). (*b*) A hexagonal input array and one rotated by 30° are subjected to a computer-simulated "imaging" with an asymmetric tip (tip shown at 3:1 magnification, orientation relative to array as shown). Particles in the resulting arrays appear better resolved when the tip asymmetry is offset 30° from the one of the threefold lattice lines. While the output images show a streaking of the array when the lattice is aligned with the tip asymmetry. The diffraction patterns from the computed Fourier transforms (*inset*) are virtually identical to those computed for the two domains in (*a*). Details of the algorithm used to compute (b) are available from the authors upon request. Bar = 50 nm.

protrusions on the nanometer scale that are sometimes called "mini-tips." Since there are not yet any reliable tip characterization procedures, it is not possible to correlate strictly tip structure with the observed connexon morphology. However, it is our experience that later-generation tips such as ion-milled EBD tips or conical silicon tips produce higher-resolution images than standard silicon nitride tips. With dozens of pyramidal silicon nitride tips that we have used we routinely see regular arrays but have not seen connexon substructure with the detail described here. Therefore we believe that our current images are limited by tip structure and that improvements in tips, one of the most active areas of AFM research today, will lead to images being routinely obtained that are as good as or better than our best results.

Another obvious effect of tip structure is the asymmetry in the arrays of connexons. Tips that produce effects like these are quite common. For example, it is known that the sides of the base of the tip defined by the mask used in the photolithographic process for manufacturing standard silicon nitride cantilevers can differ in length by up to 100 nm. This can result in a barlike structure at the apex tip, rather than a point. Except for single atom tips, it is likely that all tips have some degree of asymmetry that will result in better *xy* resolution in some directions along the surface.

Potential problems

With a new and rapidly changing technology such as atomic force microscopy, artifacts are a significant problem. At present these include damage or deformation to the sample during imaging or manipulation (such as dissection), distortion of the image by the detection system (including tip and feedback loop), and structural changes induced by the surface to which the sample is attached.

Deformation of soft biological materials during imaging with the atomic force microscope has often been seen and has been considered in the context of forces that hold biomolecules together (57). This deformation may be reversible or irreversible. It is quite common to see macromolecules such as proteins or nucleic acids move and change shape during imaging with the AFM or to see different morphologies, depending on the scan direction. Most of this deformation is likely reversible, as has been seen for the hexagonally packed intermediate layer of *D. radiodurans* (27). During dissection of the gap junction membrane there is clearly an irreversible deformation of the top membrane, and in some cases there are obvious defects in the remaining membrane (26). Despite this fairly gross deformation there is no evidence for the breaking of covalent bonds during the dissection. The forces that have to be used to intentionally break covalent bonds, such as when cutting DNA with the tip (29–31), are at least an order of magnitude greater than the forces used here. On a finer scale, the channel arrays are usually stable to repeated scanning at low force. However, even at very low force there is a slow degradation of the membrane substructure over long periods of time. This observation may be interpreted as the accumulation of small damage during each scan, although the nature of this damage is not understood.

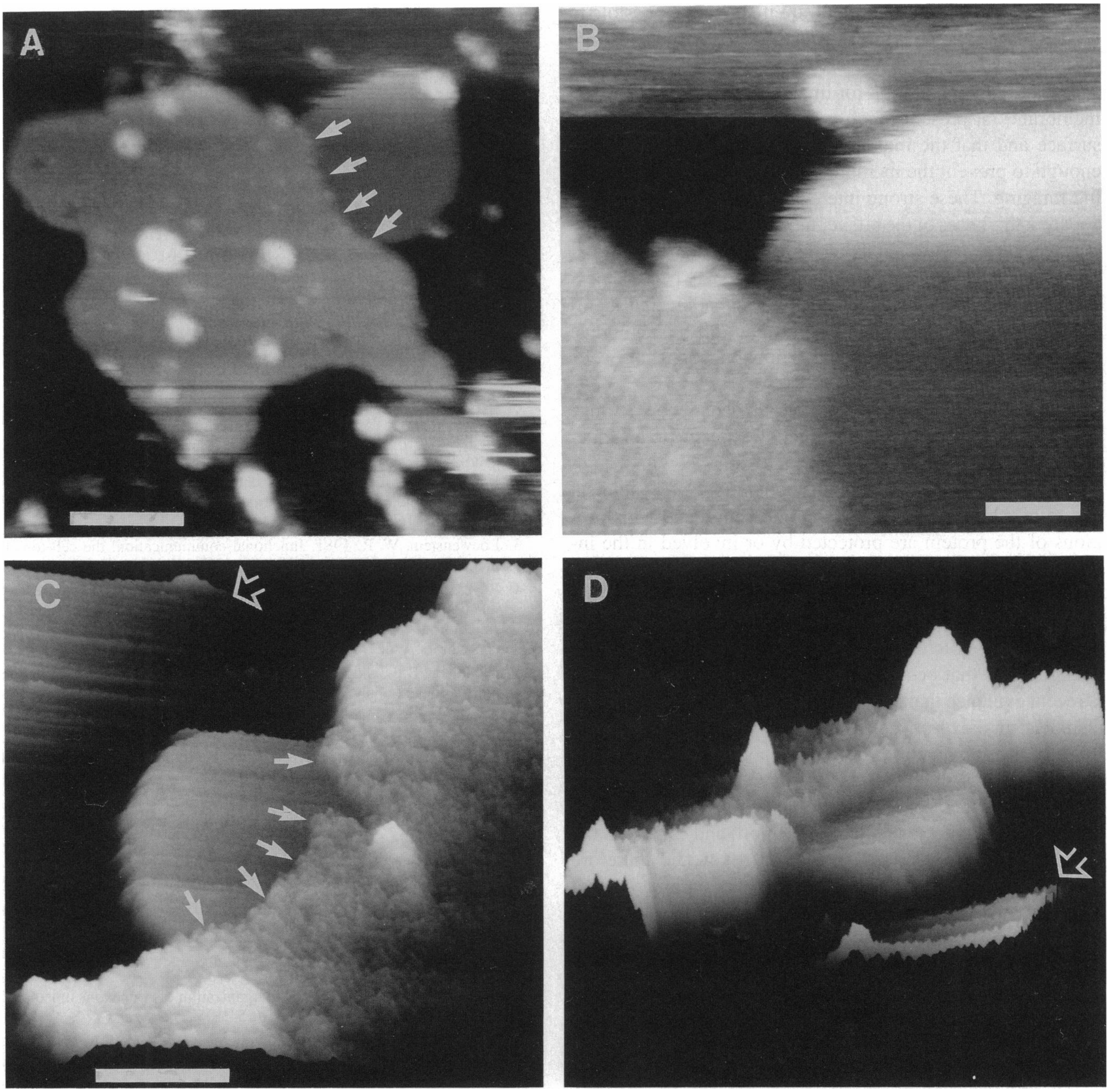

FIGURE 10 Surface of the gap junction at the border with nonjunctional membrane. (*a*) Small drop-shaped (in the plane of the membrane) regions of nonjunctional membrane are often seen at the edge of isolated gap junctions in our preparations. If these regions are large, they are often removed by the tip even at low force. However, the smaller regions shown here are stable through the dissection. (*b*) Magnification of the border (*arrows* in *a*) reveals the smooth, apparently naked lipid membrane to the right and the extracellular surface of the connexon array to the left. (*c*) A surface plot of a different nonjunctional membrane "droplet" shows the lipid membrane to the left of the border (border is marked by *arrows*) and the array channels to the right. Cross-sectional measurements across the border between junctional and nonjunctional membrane show that the connexons protrude ~1.4 nm from the lipid surface. Due to the tilt and the gray scale used, the contact between the membrane and the mica is not seen. A small piece of the mica surface does appear at the top left (*open arrow*). (*d*) The same membrane rotated and displayed as a surface plot at a 30° tilt, clearly showing the connexons protruding above the lipid membrane. (*a*) Bar = 200 nm. (*b*) Bar = 50 nm. (*c*) Bar = 100 nm.

In addition to the contribution of tip structure to images, an image can also be convoluted by the feedback loop. All of the images in this paper were acquired with the feedback loop on the microscope active, usually as high as the system would allow, and most images use the actual feedback loop signal to display height. The time constants for the feedback loop response on our microscope have not been quantified. However, it is clear from the error signal image (such as Fig. 2), where the width of the leading bright edge or trailing shadow are measures of feedback response, that these time constants are of a magnitude that could significantly affect the image. At present this contribution to the images here is not understood. In the future it should be possible to reduce this problem by integrating the error signal back into the final image.

The sample preparation for imaging isolated gap junction membranes at present requires that they be supported by a surface and that the interaction with the surface be strong enough to prevent the membrane from being dislodged during imaging. These strong interactions appear to reduce the apparent thickness of the bilayer next to the surface and could induce structural alterations of the gap junction that propagate through to the extracellular surface. It may become possible to circumvent this problem by suspending the membranes over a hole, although the elasticity of the membrane that has hampered high-resolution imaging of whole cells would have to be overcome.

A significant concern regarding the connexon surface structure described here is the effect of exposing to an aqueous environment domains that normally interact with the apposing connexon. Little is known about the specific chemical nature of the connexon-connexon interaction and which regions of the protein are protected by or involved in the interaction, although some information is available from chemical splitting experiments (58, 59). Dissection of the membrane with the AFM tip exposes these domains, which may result in structural alterations analogous to surface reconstructions that occur in many materials. However, there is recent evidence that connexins can form functional "hemichannels" in the plasma membrane with properties similar to those of the gap junction (60–62). In addition, antibodies to the extracellular domains of Cx43 have been shown by immunofluorescence to bind to nonjunctional plasma membrane (D. Laird, personal communication) and can block the formation of cell-to-cell channels (63). It would therefore appear that there are forms of the gap junction proteins that exist naturally with the extracellular domains exposed, although there is no structural information on this form of the channel.

CONCLUSION

The images described here represent the first AFM images of an individual ion channel with substantial substructure, in particular the height of individual connexons above the lipid membrane, the width of the pore at the site of connexon-connexon interaction, and height modulation of individual connexons at the connexon-connexon interaction surface. However, there are several concerns regarding artifacts and contrast mechanism that must be addressed before the full significance of these measurements is understood. The apparent tip structure-defined resolution limits of our images holds out hope for significant improvements in the near future.

The gap junction isolation method described here was developed in collaboration with Dr. James D. Hatton. We thank Hal Morrett for the ion-milled EBD tips, Mike Kirk for the generous gift of conical silicon tips, Digital Instruments for providing the microscopes used, and Jason Cleveland for computational assistance with Fig. 9. We also thank Jason Cleveland, Srin Manne, Paul Hillner, and Mark Yeager for helpful discussions, and Andreas Engel, John Badger, Ross Johnson, Paul Lampe, Dan Goodenough, David DeRosier, Helen Hansma, and Eric Henderson for critical comments on the manuscript.

This research was supported by Colvin and Merck Fellowships from the California Institute of Technology (J. H. Hoh), the Office of Naval Research (P. K. Hansma, J. H. Hoh), the A. B. Ruddock and Pfeiffer funds (J.-P. Revel), NIH grant CA47439 (G. E. Sosinsky, awarded to D. L. D. Caspar), and NIH grant GM43217 (G. E. Sosinsky). Funds to purchase and maintain the Brandeis Structural Biology computer system were obtained from NIH shared instrumentation grant 1-S10-RR04671-01 (awarded to D. J. DeRosier). The manuscript was completed with the support of a postdoctoral fellowship from the Human Frontier Science Program (J. H. Hoh, LT 438/92).

REFERENCES

1. Revel, J-P., and M. Karnovsky. 1967. Hexagonal array of subunits in intercellular junctions of the mouse heart and liver. *J. Cell Biol.* 33: C7–C12.
2. Bennett, M. V. L., and D. A. Goodenough. 1978. Gap junctions, electrotonic coupling, and intercellular communication. *Neurosci. Res. Prog. Bull.* 16:371–486.
3. Loewenstein, W. R. 1981. Junctional communication: the cell-to-cell membrane channel. *Physiol. Rev.* 61:829–913.
4. Revel, J-P., S. B. Yancey, and B. J. Nicholson. 1985. Biology of gap junction molecules and development. *In* The Cell in Contact: Adhesion Junctions as Morphogenetic Determinant. G. M. Edelman and J-P. Thiery, editors. Wiley, London. 411–425.
5. Nicholson, B. J., and J-P. Revel. 1983. Gap junctions in liver: isolation, morphological analysis, and quantitation. *Methods Enzymol.* 98:519–537.
6. Caspar, D. L. D., D. A. Goodenough, L. Makowski, and W. C. Phillips. 1977. Gap junction structures. I. Correlated electron microscopy and x-ray diffraction. *J. Cell Biol.* 74:605–628.
7. Makowski, L., D. L. D. Caspar, W. C. Philips, and D. A. Goodenough. 1977. Gap junction structures. II. Analysis of the x-ray diffraction data. *J. Cell Biol.* 74:629–645.
8. Unwin, P. N. T., and G. Zampighi. 1980. Structure of the junction between communicating cells. *Nature (Lond.).* 283:545–549.
9. Unwin, P. N. T., and P. D. Ennis. 1984. Two configurations of a channel-forming membrane protein. *Nature (Lond.).* 307:609–613.
10. Sosinsky, G.E. 1992. Image analysis of gap junctions structures. *Electron Microsc. Rev.* 5:59–76.
11. Gogol, E., and N. Unwin. 1988. Organization of connexons in isolated rat liver gap junctions. *Biophys. J.* 54:105–112.
12. Beyer, E.C., D. A. Goodenough, and D. L. Paul. 1988. The connexins, a family of related gap junction proteins. *In* Gap Junctions. E. L. Hertzberg and R. G. Johnson, editors. Alan R. Liss, New York. 167–176.
13. Dermietzel, R. 1991. The gap junction family—structure, function and chemistry. *Anat. Embryol.* 182:517–528.
14. Bennett, M. V. L., L. C. Barrio, T. A. Bargiello, D. C. Spray, E. Hertzberg, and J. C. Saez. 1991. Gap junctions: new tools, new answers, new questions. *Neuron.* 6:305–320.
15. Revel, J-P., J. H. Hoh, S. A. John, D. W. Laird, K. Puranam, and S. B. Yancey. 1992. Aspects of gap junction structure and assembly. *Semin. Cell Biol.* 3:21–28.
16. John, S. A., and J-P. Revel. 1991. Connexon integrity is maintained by non-covalent bonds: intramolecular disulfide bonds link the extracellular domains in rat connexin-43. *Biochem. Biophys. Res. Commun.* 178:1312–1318.
17. Rahman, S., and W. H. Evans. 1991. Topography of connexin 32 in rat-liver gap-junctions—evidence for an intramolecular disulfide linkage connecting the 2 extracellular peptide loops. *J. Cell Sci.* 100:567–578.
18. Hirokawa, N., and J. Heuser. 1982. The inside and outside of gap junction membranes visualized by deep-etching. *Cell.* 30:395–406.
19. Binnig, G., C. F. Quate, and C. Gerber. 1986. Atomic force microscope. *Phys. Rev. Lett.* 56:930–933.

20. Hansma, P. K., V. B. Elings, O. Marti, and C. E. Bracker. 1988. Scanning tunneling microscopy and atomic force microscopy: application to biology and technology. *Science (Washington DC)*. 242:209–216.

21. Engel, A. 1991. Biological applications of scanning probe microscopes. *Annu. Rev. Biophys. Biophys. Chem.* 20:79–108.

22. Hoh, J. H., and P. K. Hansma. 1992. Atomic force microscopy for high resolution imaging in cell biology. *Trends Cell Biol.* 2:208–213.

23. Butt, H-J., K. H. Downing, and P. K. Hansma. 1990. Imaging the membrane protein bacteriorhodopsin with an atomic force microscope. *Biophys. J.* 58:1473–1480.

24. Hoh, J. H., R. Lal, S. A. John, J. P. Revel, and M. F. Arnsdorf. 1991. Atomic force microscopy and dissection of gap junctions. *Science (Washington DC)*. 253:1405–1408.

25. Hoh, J. H., R. Lal, S. A. John, B. Drake, J-P. Revel, and M. F. Arnsdorf. 1993. Atomic force microscopy of gap junctions. *In* Progress in Cell Research. J. E. Hall, G. A. Zampghi, and R. M. Davis, editors. Elsevier Science Publishers, Amsterdam. Volume 3, 41–45.

26. Hoh, J. H., J-P. Revel, and P. K. Hansma. 1992. Membrane-membrane and membrane substrate adhesion during dissection of gap junctions with the atomic force microscope. *Proc. Society for Photo-Opticel Instrumentation and Engineering.* 1639:212–215.

27. Schabert, F., A. Hefti, K. Goldie, A. Stemmer, A. Engel, E. Meyer, R. Overney, and H-J. Günterodt. 1992. Ambient pressure scanning probe microscopy of 2D regular protein arrays. *Ultramicroscopy*. 42–44: 1118–1124.

28. Devaud, G., P. S. Furcinitti, J. C. Fleming, M. K. Lyon, and K. Douglas. 1992. Direct observation of defect structure in protein crystals by atomic force and transmission electron microscopy. *Biophys. J.* 63:630–638.

29. Henderson, E. 1992. Imaging and nanodissection of individual supercoiled plasmids by atomic force microscopy. *Nucleic Acids Res.* 20: 445–447.

30. Hansma, H. G., J. Vesenka, C. Siegerist, G. Kelderman, H. Morrett, R. L. Sinsheimer, V. Elings, C. Bustamante, and P. K. Hansma. 1992. Reproducible imaging and dissection of plasmid DNA under liquid with the atomic force microscope. *Science (Washington DC)*. 256:1180–1184.

31. Vesenka, J., M. Guthold, C. L. Tang, D. Keller, E. Delaine, and C. Bustamante. 1992. Substrate preparation for reliable imaging of DNA molecules with the scanning force microscope. *Ultramicroscopy*. 42–44:1243–1249.

32. Weisenhorn, A. L., P. K. Hansma, T. R. Albrecht, and C. F. Quate. 1989. Forces in atomic force microscopy in air and water. *Appl. Phys. Lett.* 54:2651–2653.

33. Burnham, N. A., and R. J. Colton. 1989. Measuring the nanomechanical properties and surface forces of materials using an atomic force microscope. *J. Vac. Sci. Technol.* A7:2906–2913.

34. Weisenhorn, A. L., P. Maivald, H-J. Butt, and P. K. Hansma. 1992. Measuring adhesion, attraction, and repulsion between surfaces in liquids with an atomic force microscope. *Phys. Rev. Lett. B.* 45:11226–11232.

35. Sarid, D., and V. Elings. 1991. Review of scanning force microscopy. *J. Vac. Sci. Technol. B.* 9:431–437.

36. Putman, C. A. J., K. O. van der Werf, B. G. de Grooth, N. F. van Hulst, J. Greve, and P. K. Hansma. 1992. A new imaging mode in atomic force microscopy based on the error signal. *Proc. Society for Photo-Opticel Instrumentation and Engineering.* 1639:198–204.

37. Albrecht, T. R., S. Akamine, T. E. Carver, and C. F. Quate. 1990. Microfabrication of cantilever styli for the atomic force microscope. *J. Vac. Sci. Technol. A.* 8:3386–3396.

38. Akama, Y., E. Nishimura, A. Sakai, and H. Murakami. 1990. New scanning tunneling microscopy tip for measuring surface topography. *J. Vac. Sci. Technol. A.* 8:429–433.

39. Keller, D. J., and C. C. Chou. 1992. Imaging steep, high structures by scanning force microscopy with electron-beam deposited tips. *Surface Sci.* 268:333–339.

40. Cleveland, J. P., S. Manne, D. Bocek, and P. K. Hansma. 1993. A nondestructive method for determining the spring constant of cantilevers for scanning force microscopy. *Rev. Sci. Instrum.* 64:403–405.

41. Butt, H-J., P. Siedle, K. Seifert, K. Fendler, T. Seeger, E. Bamberg, A. Weisenhorn, K. Goldie, and A. Engel. 1992. Scan speed limit in atomic force microscopy. *J. Microscopy.* 169:75–84.

42. Sosinsky, G. E., T. S. Baker, D. L. D. Caspar, and D. A. Goodenough. 1990. Correlation analysis of gap junction lattice images. *Biophys. J.* 58:1213–1226.

43. Baker, T. S., D. L. D. Caspar, C. J. Hollingshead, and D. A. Goodenough. 1983. Gap junction structures. IV. Asymmetric features revealed by low-irradiation microscopy. *J. Cell Biol.* 96:204–216.

44. Baker, T. S., G. E. Sosinsky, D. L. D. Caspar, C. Gall, and D. A. Goodenough. 1985. Gap junction structures. VII. Analysis of connexon images obtained with cationic and anionic negative stains. *J. Mol. Biol.* 184:81–98.

45. Crowther, R. A., and L. A. Amos. 1971. Harmonic analysis of electron microscope images with rotational symmetry. *J. Mol. Biol.* 60:123–130.

46. Unser, M., B. L. Trus, and A. C. Steven. 1987. A new resolution criterion based on spectral signal-to-noise ratios. *Ultramicroscopy* 23:39–52.

47. Goodenough, D. A., and W. Stoeckenius. 1972. The isolation of mouse hepatocyte gap junctions. *J. Cell Biol.* 54:646–656.

48. Henderson, D., H. Eibl, and K. Weber. 1979. Structure and biochemistry of mouse hepatic gap junctions. *J. Mol. Biol.* 132:193–218.

49. Finbow, M. E., S. B. Yancey, R. G. Johnson, and J. Revel. 1980. Independent lines of evidence suggesting a major gap junctional protein with a molecular weight of 26,000. *Proc. Natl. Acad. Sci. USA.* 77: 970–974.

50. Benedetti, E. L., and P. Emmelot. 1968. Hexagonal array of subunits in tight junctions separated from isolated rat liver plasma membranes. *J. Cell Biol.* 38:15–24.

51. Sosinsky, G. E., J. C. Jesior, D. L. D. Caspar, and D. A. Goodenough. 1988. Gap junction structures. VIII. Membrane cross-section. *Biophys. J.* 53:709–722.

52. Saxton, W. O., and W. Baumeister. 1982. The correlation averaging of a regularly arranged bacterial cell envelope protein. *J. Microsc.* 127: 127–138.

53. Sikerwar, S. S., and N. Unwin. 1988. Three-dimensional structure of gap junctions in fragmented plasma membranes from rat liver. *Biophys. J.* 54:113–119.

54. Malewicz, B., V. V. Kumar, R. G. Johnson, and W. J. Baumann. 1990. Lipids in gap junction assembly and function. *Lipids.* 25:419–427.

55. Israelachvili, J. N. 1992. Intermolecular and Surface Forces. 2nd Ed. Academic Press, New York.

56. Makowski, L. 1985. Structural domains in gap junctions: implications for the control of intercellular communication. *In* Gap Junctions. M. V. L. Bennett and D. C. Spray, editors. Cold Spring Harbor Laboratory, Cold Spring Harbor, NY. 5–12.

57. Persson, B. N. J. 1987. The atomic force microscope: can it be used to study biological molecules? *Chem. Phys. Lett.* 141:366–368.

58. Manjunath, C. K., G. E. Goings, and E. Page. 1984. Detergent sensitivity and splitting of isolated liver gap junctions. *J. Membr. Biol.* 78: 147–155.

59. Goodenough, D. A., and N. B. Gilula. 1974. The splitting of hepatocyte gap junctions and zonulae occludentes with hypertonic disaccharides. *J. Cell Biol.* 61:575–590.

60. DeVries, S. H., and E. A. Schwartz. 1992. Hemi-gap junction channels in solitary horizontal cells of the catfish retina. *J. Physiol.* 445:201–230.

61. Paul, D. L., L. Ebihara, L. J. Takemoto, K. I. Swenson, and D. A. Goodenough. 1991. Connexin46, a novel lens gap junction protein, induces voltage-gated currents in nonjunctional plasma-membrane of *Xenopus* oocytes. *J. Cell Biol.* 115:1077–1089.

62. Beyer, E. C., and T. H. Steinberg. 1991. Evidence that the gap junction protein connexin-43 is the ATP-induced pore of mouse macrophages. *J. Biol..Chem.* 266:7971–7974.

63. Meyer, R. A., D. W. Laird, J-P. Revel, and R. G. Johnson. 1992. Inhibition of gap junction and adherens junction assembly by connexin and A-CAM antibodies. *J. Cell Biol.* 119:179–189.